UNIVERSITY of CALIFORNIA
SANTA CRUZ

X-RAY-OPTICAL SCALING RELATIONS FOR THE DARK ENERGY SURVEY Y3 REDMAPPER CLUSTERS

A thesis submitted in partial satisfaction of the
requirements for the degree of

BACHELOR OF SCIENCE

in

ASTROPHYSICS

by

Jose Elias Jobel

28 August 2020

Abstract

X-RAY-OPTICAL SCALING RELATIONS FOR THE DARK ENERGY SURVEY Y3 REDMAPPER CLUSTERS

by

Jose Elias Jobel

Studies of galaxy clusters have proven successful cosmological probes. They are known to be the largest structures to have become gravitationally stable and enter into a state of virial equilibrium allowing us to infer valuable information about dark energy. Thus we are interested in analyzing clusters identified in the Dark Energy Survey Y3 (DES Y3) and work toward placing strong constraints on the dark energy equation of state parameter, ω_λ by analyzing the number density of galaxy clusters across a range of redshifts as a function of cluster mass. Given the fact that direct measurement of cluster mass is not yet possible, here in this work we look at the correlation of richness for clusters in DES Y3 with X-ray temperatures and X-ray luminosities which relate to cluster mass, where richness is the number of galaxies within a cluster. We introduce the **Clu**ster **S**caling **R**elation (CluStR) fitting algorithm responsible for calculating scaling relations between observables by incorporating the Bayesian approach developed by Brandon Kelly. Finally, we then present our results as the following; an r_{2500} T_X-λ scaling relation of $\ln(E(z)^{-2/3} k_B T_{X,r2500}) = (0.38 \pm 0.06) \ln(\frac{\lambda}{98}) + 1.92 \pm 0.02$ results for 167 'detected' clusters with an intrinsic scatter $\sigma_{intr} = 0.28 \pm 0.02$ and an r_{2500} L_X-λ scaling relation of $\ln(\frac{L_{X,r2500}}{E(z)10^{44}}) = (1.19 \pm 0.14) \ln(\frac{\lambda}{98}) + 0.64 \pm 0.07$ results for 167 'detected' clusters with an intrinsic scatter $\sigma_{intr} = 0.89 \pm 0.05$.

Contents

List of Figures

List of Tables

To my parents,

Delmy Diaz and Jose Elias Jovel

Acknowledgements

I'd like to start by thanking my parents for the unconditional love and support they have provided throughout my 25 years on this earth. Every decision I have shared with them has never met a rejection or a thought of doubt. They have sacrificed goals, dreams, sleep, happiness, and so much more to see that I live the dream they dreamt for themselves. I want to thank my beautiful grandmother, Ana Diaz, for her love knows no limit. Her belief in me fuels my motivation to thrive in anything I set my mind to. To my two younger sisters, I want to thank them for allowing me to be the person who inspires them to reach for the stars. I want to thank the following people in no particular order; my aunt, Elvira Diaz, for the precious love she has for me and for the countless reminders to never stop reaching for more or else I would feel the full power of her rage; my aunt, Blanca Cea, for the priceless wisdom she offers me in both my darkest and proudest moments; my uncle, Alfredo Diaz, who aside from my father has taught me at a very young age how to work hard under the sun, teaching me the resilience my grandfather taught him. I want to also thank my cousins for their a incredible belief in me. It brings me joy to know that each and every one of them is proud of my progress.

The work presented here would not have been possible without the priceless opportunity Professor Tesla Jeltema allowed me to be a part of. An opportunity that has been the most rewarding of anything I could have thought possible for myself. The unwavering care she has provided throughout my time working with her is something I truly am grateful for and is a quality I will implement when my time comes to take on the role of a mentor. Professor Tesla, I would like to thank you for making my time at the University of California, Santa Cruz an exceptional one, for teach me about the incredible work you do, and sharing your genuine excitement for the forward steps I take in completing the tasks you've entrusted me with. You have given me the opportunity to make my family proud of the work I've done along side your group, for that I am forever grateful.

My research experience would not have made it this far without the out-

standing knowledge and guidance of Spencer Everett. His ability to simplify and teach complex computer algorithms have allowed me to grow in my research experience and apply what I have learned to the work presented here. For this reason along with many others, I thank you very much Spencer.

To all my high school friends, I finally did it. To my community college friends, thank you for spending countless hours in the MESA basement with me while we motivated each other to learn the material at hand. I would not have made it this far without learning from each and everyone one of you. To my Santa Cruz friends, thank you for the beautiful memories and lifelong friendships. To my fellow physics friends and future colleagues Adam Duran, Taylor Lewis, Paige Kelly, and Eric Matteini thank you for your continual support, for the team building exercises during our video game sessions, for sharing your research enthusiasm, for sharing hilarious physics memes, and most notably thank you for pushing me to become more knowledgeable than I was yesterday.

Last, but absolutely not least, I want to acknowledge the single most influential person in my life, my late grandfather Andres Diaz. Words can't describe the enormous influence he has had in the 'what if', 'should I', 'can I', 'would this' and 'I'll try' decisions I have faced. Every challenge and opportunity that has presented itself to me will always be met with the mindset he instilled in me during his time with us. His presence in my life was profound.

1

Introduction

The Lambda Cold Dark Matter model, also known as ΛCDM, is the current accepted cosmological model described by General Relativity and the Friedman-Lemaître-Walker (FLRW) equations. The model describes a flat accelerating universe mainly dominated by unknown forms of matter and energy. The two are referred to as dark matter and dark energy, respectively. While their physical mechanisms are not fully understood yet, the effects they have on our Universe are evident. For example, dark matter making up roughly 25% of our cosmos is predicted to be composed of a non-relativistic (cold) non-baryonic form of matter whose gravitational potential plays an important role in the hierarchical formation of large scale structures (Voit, 2005; Frieman et al., 2008). Furthermore, 70% of our cosmos is dark energy whose effects are associated with negative pressure responsible for the current dominating expansion rate of our Universe (Abbott et al., 2019). Dark energy has influenced the structural growth from the smallest objects to large scale structures by influencing the rate at which the Universe expands. For this reason coupled with the fact that formation of structures is hierarchical, clusters of galaxies are understood to be the most recent gravitationally stable objects that can provide valuable information about dark energy. Thus, are powerful probes in understanding the underlying cosmology. As an illustration, consider our universe having contained a greater quantity of dark energy content in the past. Under this condition, the expansion due to dark energy would force clusters of galaxies to form

much earlier to reach their current number density. For this reason, studying the number density of galaxy clusters across a range of redshifts as a function of cluster mass can provide valuable information of how much dark energy was present throughout time. As a result, we are interested in observables that directly relate to cluster mass.

Galaxy clusters are great X-ray sources due to their deep potential wells trapping ionized hydrogen and helium. The large collection of ionized particles are in a plasma phase spanning throughout the cluster called the **I**ntra**C**luster **M**edium (ICM). Temperatures within the ICM reach between 10^7 - 10^8 Kelvin causing particles to emit thermal energy in the form of X-ray emission (Böhringer & Werner, 2010). The ICM being the "hottest thermal equilibrium plasma" as stated by Böhringer and Werner 2010 paper on X-ray spectroscopy of galaxy clusters, provides many observables relating to cluster mass. It is imperative to keep in mind that for any observable-mass or observable-observable relation there will be an intrinsic scatter distribution associated which will be important to quantify.

This thesis will go into detail about the motivation for the CluStR program, which incorporates a statistical Bayesian approach developed by Brandon Kelly (2007). In section 1, I provide the general motivation to pursue the relationship between cluster observables and cluster mass. In section 2, I describe galaxy cluster formation along with cluster observables and their use for constraining cosmological parameters. Section 3 will cover a brief overview of the Dark Energy Survey and discuss the cluster finder program which outputs cluster candidates used for X-ray analysis known as **r**ed-sequence **M**atch-filter **P**robabilistic **P**ercolation (redMaPPer). In the same section I describe the **M**ass **A**nalysis **T**ool for **C**handra (MATCha) X-ray analysis pipeline, a pipeline previously used to analyze the Sloan Digital Sky Survey (SDSS) Data Release 8 (DR8) data set presented by Hollowood et al. (2018). In section 4, I introduce the **Clu**ster **S**caling **R**elation (CluStR) fitting algorithm responsible for calculating various scaling relations by incorporating the Bayesian Approach developed by Brandon Kelly which implements measure-

ment errors, intrinsic scatter, and gaussian mixture modeling for the covariates. In the same section, I present the derived scaling relations results. Finally, Section 5 provides a summary of this work and future upgrades to CluStR.

2

Cosmology with Clusters

Governed by Hubble's Law, the history of large-scale structures of our universe can be traced back to regions of space where perturbations in the density distribution within these region exceeded the mean density of the Universe from which gravitational attraction between small-scale clumps of matter collected to form larger structures (Voit, 2004; Allen et al., 2011). These objects then decoupled from the expansion, collapsed to form galaxies, and eventually collected into clusters of galaxies whose structures fell into a state of virial equilibrium (Voit, 2004). Further understanding of this hierarchical process requires numerical simulations due to the fact that spherically symmetric models of cluster formations are not enough to fully describe the accretion process in clusters and is a topic outside the scope of this work. For further details on cluster formation see, e.g., (Diaferio & Geller, 1997; Voit, 2004; Allen et al., 2011; Kravtsov & Borgani, 2012).

Although clusters of galaxies are complex structures that include a mix of baryonic matter and non-relativistic (cold) non-baryonic matter, clusters have proven themselves to be an outstanding source of information from aiding the establishment of our standard model of cosmology to providing ways to test models of galaxy formation and the thermodynamics of the intergalactic medium. Our first known encounter with galaxy clusters date back to Charles Messier (1784) and William Herschel (1785) both of whome introduced to the world two now well studied clusters, the Virgo and Coma clusters. About two centuries later, the first cluster

catalog was published by George Abell (1957) that contained 1682 selected clusters of galaxies identified within the optical sky survey provided by the National Geographic Society of Palomar Observatory Sky Survey (Abell, 1957). Each cluster in Abell's catalog was purposefully selected for inclusion in several statistical analyses. In more recent times, sophisticated tools are developed to help identify and analyze potential clusters by creating automated pipelines such as the two discussed in this paper. The first of the two tools is the **r**ed-sequence **M**atched-filter **P**robabilistic **P**ercolation (redMaPPer) algorithm responsible for identifying cluster candidates from large optical surveys such as the one provided by the Dark Energy Survey Collaboration and the second is the **M**ass **A**nalysis **T**ool for **Cha**ndra (MATCha) pipeline responsible for X-ray image analysis, both covered in detail in Section 3. I provide below a brief summary covering cluster observables obtained through optical and X-ray wavebands, while attempting to emphasize their importance to this work.

2.1 Optical Observables

Within galaxy clusters, spectroscopic data from galaxies allow the determination of cluster mass through studying galaxy dynamics (Voit, 2004). For instance, assuming a cluster has been optically identified, one can measure the velocity distribution of galaxy clusters from redshift data alone which help reduce projection effects and estimate the cluster's mass. Applying this analysis to real clusters has proven difficult to employ given that the velocity fields become irregular within regions of increased particle kinetic energy implying the velocity dispersion distributions are non-linear (Diaferio & Geller, 1997), (Voit, 2004).

Another advantage in working with optical data is the accessibility to a cluster's photometric redshift. In this work, cluster redshift emerges from the color distribution obtained from multi-band imaging. This is done by exploiting the fact that many cluster centers contain galaxies that have reached the end of their star formation, leaving for us to see a color distribution from which we can deduce redshift

estimates (Gladder & Yee, 2005; Gilbank et al., 2011; Bell et al., 2004). To do this, one needs a red sequence model to fit individual galaxies and in return we obtain a richness observable λ that correlates tightly with cluster mass (Rykoff et al., 2014). Although the definition of richness varies, here we refer to λ as a variable quantity that estimates the number of red-sequence galaxies within a cluster (Hollowood et al., 2018; Rykoff et al., 2014).

2.2 X-ray Observables

Galaxy clusters as stated before are important stable astrophysical structures providing astronomers as well as cosmologists with cosmic-scale laboratories in which we can study regions where the cluster's gravitational potential well traps hot plasma and raises temperatures up to 10^7 - 10^8 Kelvin causing particles to emit thermal energy in the form of X-ray emissions. Called the **I**ntra**C**luster **M**edium (ICM), the plasma filling clusters contains three important X-ray collisional mechanisms: free-free emissions (Bremsstrahlung radiation) caused by electric fields of near by charged particles; free-bound emissions (recombination radiation); and bound-bound emissions (Allen et al., 2011; Hollowood, 2018; Sarazin, 1988). Given that all three processes are proportional to the electron density squared sets up the concentrated X-ray brightness profiles of a cluster as ideal targets for well equipped telescopes such as the Chandra X-ray Observatory who possesses high-resolution imaging and spectroscopy, enabling us to compute X-ray temperatures and X-ray luminosities (Voit, 2005).

Being the only X-ray luminous, spatially extended, and gravitationally stable structures in the universe, clusters of galaxies as we have briefly reviewed provide several multi-band observables for constructing cluster catalogs. Rich catalogs as those used in this paper, prove important to the underlying cosmological work presented in this paper because help us understand cluster selection and mass.

3

Sample Selection and Analysis

3.1 The Dark Energy Survey

The Dark Energy Survey (DES) is a collaborative effort working toward placing strong constraints on the dark energy equation of state parameter, ω_λ, shedding light on the most pressing question: What is dark energy? DES is composed of two surveys: a wide-field survey and a narrow time-domain survey. Covering 5000 deg^2 of the southern sky, the wide-field survey encompasses the 2500 deg^2 of sky previously surveyed by the South Pole Telescope (SPT) Sunyaev-Zel'dovich effect (SZE) survey while making use of g, r, i, z and Y filters. Each section of the sky is observed ten times in each band, the added exposure time allows for the faintest galaxies to be detected. The aim of the wide-field survey is to detect more than 100,000 galaxy clusters with photo-z measurements to redshifts z$\geq$1 and positions for more than 300 million galaxies (The Dark Energy Survey Collaboration, 2005). The time-domain survey on the other hand focuses on covering 27 deg^2 of the same area of the sky, allowing for light curve measurements of active galactic nuclei, SNe Ia, core-collapse SNe, along with other varying celestial bodies (The Dark Energy Survey Collaboration, 2005).

From its conception in late 2003, DES submitted a proposal to build the Dark Energy Camera (DECam), a new advanced wide-field survey instrument to be mounted onto the already existing optimally configured V.M Blanco 4m telescope in Cerro Tololo Inter-American Observatory (Flaugher et al., 2015). The main com-

ponents of DECam include a 519 megapixel optical CCD camera, a 5-band g, r, i, z, and Y filter system, and a data acquisition and instrument control system to connect with the Blanco telescope (Flaugher et al., 2015). With this instrument, DES provides the astronomical community with the necessary data to place constraints on the dark energy equation of state parameter, ω_λ. DES possesses a unique approach that exceeds the redshift reach of previous successful photometric surveys such as the Sloan Digital Sky Survey (SDSS) and the Red-sequence Cluster Survey-2 (RCS-2) (Gilbank et al. 2014) making it a great resource for cluster cosmology.

3.2 The redMaPPer Pipeline

From identifying overdensities of galaxies as clusters to estimating cluster richness, optical cluster-finding algorithms have found their way to becoming an essential tool that make use of the photometric data collected by surveys such as in DES. In 2014, the **r**ed-sequence **M**atched-filter **P**robabilistic **P**ercolation (redMaPPer) algorithm was introduced by Rykoff et al., (2014) as a photometric red-sequence cluster finder based on the richness estimator developed in Rozo et al. (2009) and Rykoff et al. (2012). It is a two-stage pipeline: a calibration stage and a cluster-finding stage.

3.2.1 The Calibration Stage

Although redMaPPer relies only on the red sequence modeling approach, it first uses a large sample of galaxies with known spectroscopic redshifts to empirically calibrate the red sequence as a function of redshift. Each sample galaxy is therefore used as a guide to find nearby overdensities of galaxies with similar optical color (Rykoff et al. 2014). The process is iterated several times until we obtain a reliable set of galaxy overdensities that are used as training clusters. These clusters are then used to fit a linear red sequence model to all probable cluster members in the DES catalog.

3.2.2 The Cluster-Finding Stage

Having obtained our calibrated red sequence model, the cluster finding process begins with the assumption that each photometric galaxy in the DES catalog is a cluster center. To determine an appropriate cluster redshift z_λ, all center galaxy (CG) candidates with an overly dense population of nearby galaxies will be assigned an initial cluster redshift estimate z_{red}, where "red" denotes we are using a red sequence galaxy model (Rykoff et al. 2014). From this initial estimate, redMaPPer calculates a cluster richness λ along with correlated membership probabilities. Galaxies with the highest membership probability are then selected to re-estimate a new redshift by maximizing a likelihood function. This process is iterated until convergence. The process continues by rank-ordering each potential cluster according to likelihood.

This ranked catalog now goes through the percolation phase that begins with the highest ranked cluster C_j by recalculating z_λ and λ. It then determines a galaxy as a cluster's center with an accompanying centering probability P_{center}. Note that a given galaxy in a cluster can be a center, satellite, or a non-cluster member (Rykoff et al. 2014). Based on the determined center galaxy, the final z_λ and λ are calculated. redMaPPer now moves on to the probabilistic percolation step of this phase and updates the catalog by masking out galaxies according to membership probabilities. Finally, all low ranking cluster centers with a membership probability greater than 50% are removed from the cluster C_j population. The above process is repeated for the next ranked cluster C_{j+1} in the catalog.

The output of this pipeline is a full cluster catalog that provides essential data to this work such as cluster redshifts z_λ, cluster richness λ, and centerings.

3.3 The MATCha Pipeline

As mentioned before, the intrinsic scatter distribution associated with observable-mass or observable-observable scaling relations is a large source of uncertainty but one can quantify this intrinsic scatter by following up optically-selected

clusters with X-ray data which improve our effort to place strong cosmological constraint on the dark energy equation of state parameter, ω (Hollowood et al., 2018; Wu et al., 2010). The X-ray data used in this section is collected by one of NASA's 'great observatories', the Chandra X-ray Observatory space telescope and processed by the Chandra X-ray Center (CXC) dually managed by the Smithsonian Astrophysical Observatory (SAO) and the Massachusetts Institute of Technology (MIT) (Weisskopf et al., 2000). The Chandra X-ray Center is responsible for high-level data processing, data archiving, making the data public, and providing the analysis tools essential for the **M**ass **A**nalysis **T**ool for **Cha**ndra (MATCha) pipeline introduced by Hollowood et al. (2018). MATCha is an automated algorithm that employs several Chandra Interactive Analysis of Observations (CIAO) tools developed by CXC in order to measure X-ray temperature (T_X), X-ray luminosity (L_X), cluster centroids, and r_{500} and r_{2500} radii as a follow-up for clusters that are found in both the redMaPPer catalog and the Chandra archived data.

Similar to redMaPPer, MATCha can be described by two stages; a data preparation stage and a cluster analysis stage. The data preparation is a relatively short stage, which begins by obtaining a set of celestial coordinates (right ascension, declination) along with corresponding redshift (z_λ) from the redMaPPer cluster catalog and cross checks with the Chandra archive using the $find\_chandra\_obsid$ CIAO tool for any cluster images with the given RA and Dec. Once an image at those coordinates is found, it is downloaded and reprocessed using the *chandra_repro* CIAO tool. MATCha then applies the *deflare* CIAO tool to remove flares from lightcurves and separately reduces the energy range to 0.3-7.9keV before creating images and exposure maps for each observation (Hollowood et al., 2018). As a final step in the data preparation stage, probable point sources are identified and removed from images by employing the *wavdetect* CIAO tool, which repeatedly searches for correlation between source pixels and "Mexican-Hat" wavelet functions of various scales set by the user.

MATCha is now ready for the cluster analysis stage which focuses on de-

termining X-ray temperature, X-ray luminosity, and X-ray centroids within a 500 kpc regions, from which two radii are calculated, r_{2500} and r_{500}. For future reference, an r_{2500} region is defined to be the radius around a cluster halo where the average density is 2500 times denser than the critical density of the universe. Similarly, an r_{500} region is defined to be the radius around a cluster halo where the average density is 500 times denser than the critical density of the universe. The procedure is as follows: First, a 20 iteration attempt to find an X-ray centroid within a 500 kpc region is initiated by using the redMaPPer cluster center as its initial estimate. Each iteration continues such that the 500 kpc region is moved until a new center is found within 15 kpc of the previous center, iteration is then stopped. However, if the maximum 20 iteration limit is reached without converging to a center, then the cluster is marked 'undetected'. This 'undetected' cluster is assigned an L_X upper limit using the redMaPPer center and a 500 kpc radius. If MATCha is able to converge on an X-ray centroid within 15 kpc, it then verifies if the signal-to-noise ratio is greater than 5.0. If the latter is true, then the cluster is marked as 'detected', but if false, the cluster is marked 'undetected' and an L_X upper limit is assigned using the X-ray centroid position and the 500 kpc radius.

For each detected source, MATCha proceeds by obtaining a background-subtracted spectrum within 500 kpc radius. An assumed galactic absorption column density, nH, is calculated and the background-subtracted spectrum used to fit T_X and L_X using the XSPEC HEASARC tool. Note that nH is calculated through the HEASOFT tool (Hollowood et al., 2018). An initial r_{2500} is calculated from the 500 kpc T_X. Additionally, an iterative step is taken to converge on a new centroid within the r_{2500} region. If successful, a new background-subtracted spectrum is calculated and used to find r_{2500} T_X and L_X. If the spectral fit within the 500 kpc region fails, MATCha will use the L_X - T_X relation to repeatedly attempt to compute a T_X with an assumed 3.0 keV starting temperature along with a corresponding L_X until convergence. The r_{500} region is found starting from the r_{2500} T_X and iterating using the same steps as for the r_{2500} region. This concludes MATCha's cluster analysis

stage. Figure 3.1 shows a standard MATCha output after the above process is complete.

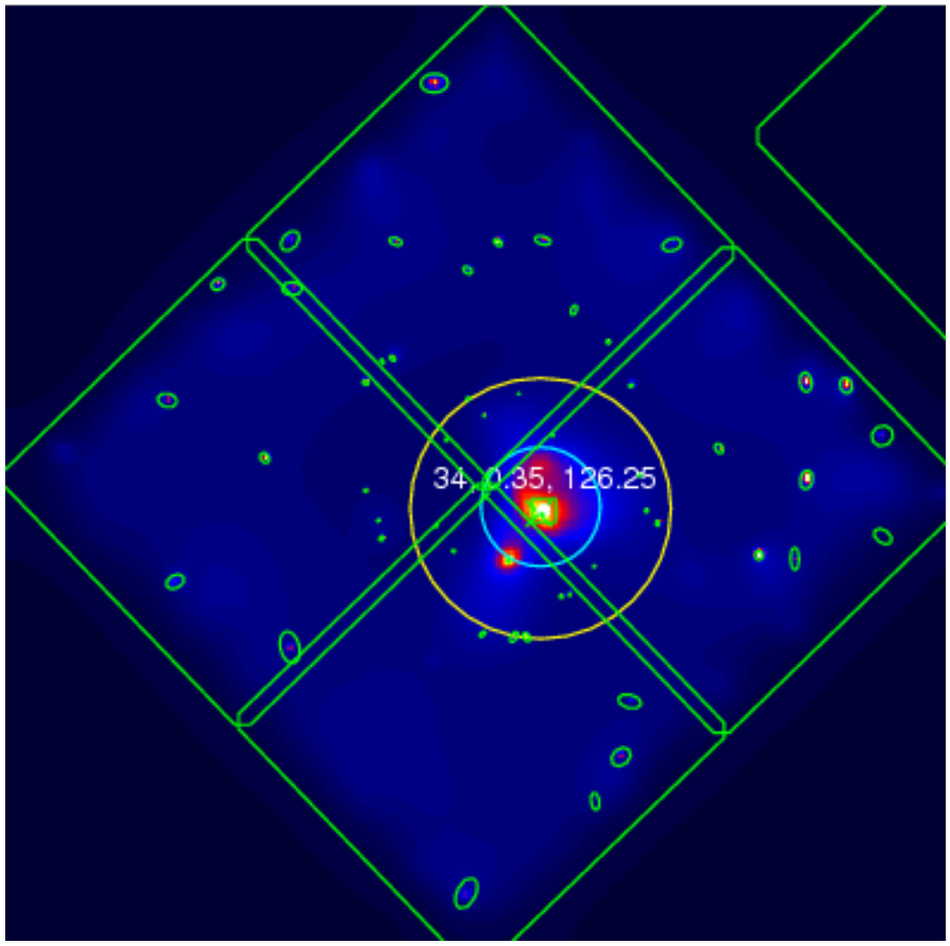

Figure 3.1: This is an example of a final MATCha processed Chandra image located at the redMaPPer celestial coordinates. The image is uniquely identified by the following; Mem_Match_Id 41, z $\approx$ 0.35, and Obsid 17185. The yellow circles represent the r_{500} radius. The cyan circle represents the r_{2500} region. The pink circle which nearly over laps with the r_{2500} region represents the 500 kpc radius. The green box at the center of each circle is placed by MATCha and represents the center of the redMaPPer cluster candidate. The green 'x' is placed on the location of the X-ray centroid (see section 3.3). The green double lines making up the four smaller squares are the CCD chip edges along with the green lines encompassing the four squares are chip edges as well. Finally, the green ellipsoids mark X-ray point sources.

4

CluStR Analysis of the Dark Energy Survey Y3 redMaPPer Catalog

Linear regression methods for analyzing astronomical data have been characterized for their ability to measure the measurement errors in the independent and dependent variable, but also for their ability to quantify the intrinsic scatter about the regression line (Kelly, 2007; Gelman et al., 2014; Akritas & Bershady, 1996). There are many commonly used algorithms in astronomy such as the FITEXY routine (Press et al., 1992) based on a linear least-squares fitting approach when only measurement errors are present or the **B**ivariate **C**orrelated **E**rrors and intrinsic **S**catter (BCES) estimator (Akritas & Bershady, 1996) method for applying linear regression analysis when intrinsic scatter and measurement errors are present. In this paper we use the **C**luster **S**caling **R**elation (CluStR) fitting algorithm which focuses on the importance of fitting a regression model to data that has heterscedastic measurement errors, probable correlation measurement errors between variables, and intrinsic scatter in the regression relation by employing the hierarchical Bayesian model proposed by Brandon Kelly (2007). The method accounts for multiple independent variables, selection effects, and most notably non-detections. Here non-detections refers to data points whose value could not be determined and have upper

and/or lower limits placed on them (Kelly, 2007). Non-detections are also known as 'censored data'. Additionally, this method has an underlying focus on deriving a likelihood function in the specific case when the intrinsic distribution of the independent variable can be described by a Gaussian mixture model.

To understand the parameters in our statistical model, we need to compute a posterior distribution. An important feature of CluStR is the inclusion of the Gibbs sampler algorithm proposed in Kelly (2007) which uses a Markov chain simulation (also known as Markov Chain Monte Carlo or MCMC) method to converge to a desired posterior distribution. The Markov chain is formed through a sequence of random walks in parameter space where each newly drawn value of the model parameter ν_i is iteratively simulated and depends on the previously drawn value ν_{i-1} (Gelman et al., 2014; Kelly, 2007; Press et al., 2007). Each value of ν is saved and the above process is iterated until the Markov chain simulation converges. The default iteration ranges from a minimum of 5,000 to a maximum of 10,000 steps. We opt for this method not only for the Markov chain property but for the reason that each new value of ν is improved at each step of the iteration process, thus converging to the desired posterior distribution.

In the final process, CluStR derives a scaling relation of the form ln(y)=α ln($\frac{\lambda}{\lambda_{piv}}$) + β. In general, the variable y can be an normalized X-ray observable T_X or L_X, α is the slope of the regression line, β is the intercept of the fit, and the parameter λ_{piv} represents the pivot point of the fit. Figure 4.1 and Figure 4.2 show the results of the analysis of the DES Y3 MATCha catalog.

4.1 Results

Our initial Dark Energy Survey Y3 redMaPPer catalog contained an approximate 53,600 potential clusters. Once this catalog was passed through the MATCha pipeline, only 1,092 clusters were found within the Chandra archived observations across a redshift range of $0.10 < z < 0.95$. The cluster sample used for the T_X-λ CluStR analysis consists of 352 'detected' clusters out of the 1,092 that

were found. Out of the 1,092, 740 clusters fell within the 'undetected' category. From the 352 'detected' clusters, the following clusters were removed from the sample due to flags: 15 clusters removed were removed because their r_{500} region was contaminated by another cluster, 7 clusters removed due to contamination in the r_{2500} region by another cluster, 27 clusters removed due to similar contamination of their background, 39 clusters removed as a result of 'masking' (a foreground or background cluster was detected instead of the target redMaPPer cluster), 9 clusters removed due to 'bad mode', 47 clusters removed due to their r_{500} radius extending outside a chip edge, 41 clusters removed due to their r_{2500} radius extending outside a chip edge. Keep in mind that a cluster can fail multiple flags. A total of 185 'detected' clusters were removed from the scaling relation sample due to flagging. This leaves us with a 'clean' sample of 167 'detected' clusters that were not flagged for the above reasons.

4.1.1 T_X - λ Scaling Relation

To understand the relation between X-ray temperature and cluster richness within an r_{2500} aperture, we rely on employing the CluStR fitting algorithm on the 167 'detected' clusters while comparing our results to those found in Hollowood et al. (2018). In our analysis we derive the following relation in the $0.10 < z < 0.95$ range,

$$\ln(E(z)^{-2/3} k_B T_{X,r2500}) = (0.38 \pm 0.06) \ln(\frac{\lambda}{98}) + 1.92 \pm 0.02 \tag{4.1}$$

and an intrinsic scatter of σ_{intr} =0.28±0.02. Here we use the Hubble parameter $E(z) = H(z)/H_0$ to normalize the temperature measurements made within a critical overdensity region (Allen et al., 2011). k_B is the Boltzmann constant. The pivot point of the fit is located at λ_{piv}=98. This is where the scatter about the regression line is a minimum. See Figure 4.1 and Figure 4.2 for plots of the $r_{2500} T_X$ - λ relations.

We now compare our r_{2500} T_X-λ relation to that in Hollowood et al. (2018) which use 235 'detected' SDSS DR8 redMaPPer clusters in their analysis. This is about 40% larger than the sample size used in this paper. The relations are analyzed

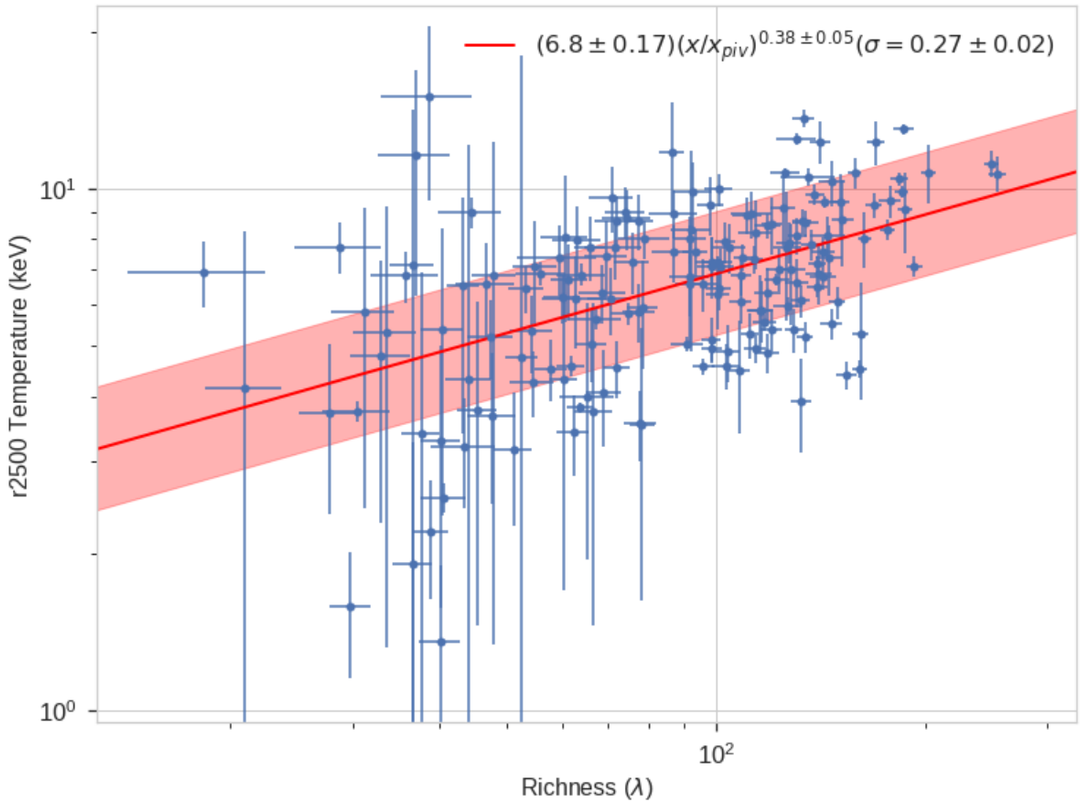

Figure 4.1: $r_{2500}\mathrm{T}_X$ - λ relation derived from a sample set of MATCha clusters using CluStR. The red translucent bar indicates the intrinsic scatter about the regression line. Here 'x' in our case refers to the richness λ input. The 'x_{piv}' refers to the pivot point calculated as the median of λ, producing a $\lambda_{piv} = 98$.

within two redshift ranges. For the r_{2500} T_X-λ in the $0.1< z <0.35$ range, the

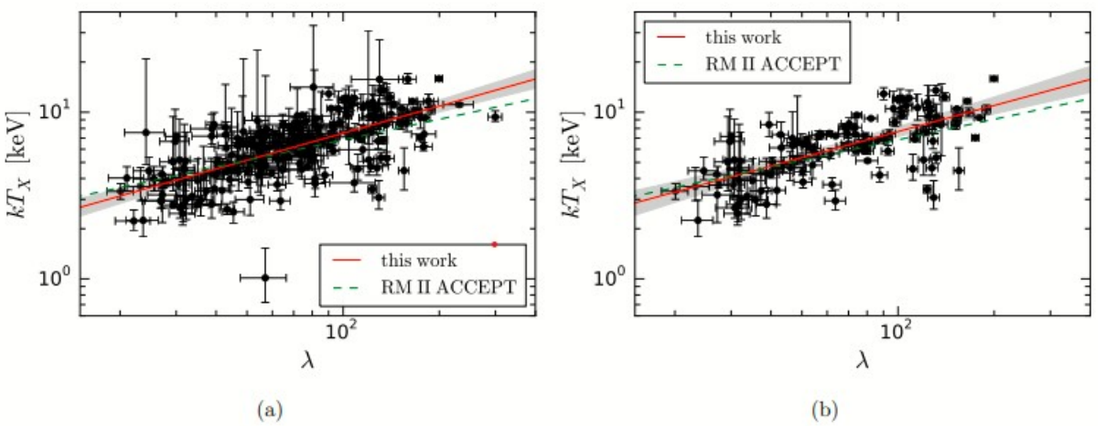

Figure 4.2: (a) r_{2500} T_X-λ scaling relation derived from SDSS DR8 cluster sample (Hollowood et al., 2018) which include clusters of all redshifts. (b) Similarly, these are clusters of redshift $0.1 < z < 0.35$. The grey translucent bar indicates the 1σ uncertainties. The red line represents the regression line, while the black points are cluster data. Note the green dashes represent the scaling relation fit on the Chandra ACCEPT cluster catalog presented in Rozo & Rykoff (2014). This figure was taken from Hollowood et al. (2018).

relation is

$$\ln(E(z)^{-2/3} k_B T_{X,r2500}) = (0.52 \pm 0.05) \ln(\frac{\lambda}{70}) + 1.85 \pm 0.03 \tag{4.2}$$

with an intrinsic scatter of σ_{intr}=0.27±0.02, comparable to the intrinsic scatter in our analysis. The second relation is examines across all redshift range providing an equation of that does not deviate significantly from Eq (4.2),

$$\ln(E(z)^{-2/3} k_B T_{X,r2500}) = (0.54 \pm 0.04) \ln(\frac{\lambda}{70}) + 1.82 \pm 0.02 \tag{4.3}$$

and has an intrinsic scatter of σ_{intr}=0.26±0.02.

We note the slope difference is less than 3σ. For a summary comparison of the model parameter results see Table 4.1.

Catalog	**Relation**	**Redshift Range**	$\boldsymbol{\alpha}$	$\boldsymbol{\beta}$	$\boldsymbol{\sigma_{intr}}$	**Figure**
DES Y3	T_X-λ	0.10< z <0.95	0.38±0.06	1.92±0.03	0.28±0.02	4.1
SDSS DR8	T_X-λ	All redshift	0.54±0.04	1.82±0.02	0.26±0.02	4.2 (a)
SDSS DR8	T_X-λ	0.1< z <0.35	0.52±0.05	1.85±0.03	0.27±0.02	4.2 (b)

Table 4.1: Here we present fit parameters to the scaling relation $\ln(E(z)^{-2/3}\ k_B\ T_X)=\alpha\ \ln(\frac{\lambda}{\lambda_{piv}})\ +\ \beta$ for two separate datasets within an r_{2500} region. T_X has units of keV. We also present the redshift range in which each cluster sample set falls within. Note σ_{intr} is the standard deviation of the intrinsic scatter. Our results are compared to those of Hollowood et al. (2018).

4.1.2 L_X - λ Scaling Relation

Similarly, the scaling relation analysis between X-ray luminosity and richness was performed using CluStR. We run the same flags cuts on the initial 352 'detected' clusters, which result in removing 185 clusters due to flaggings. This leaves us with a 167 cluster sample, a similar size to the one used for the T_X - λ analysis but still much smaller than 235 clusters used in the Hollowood et al.(2018) L_X - λ analysis. The reason for the size equivalence in samples has to due with our choice of not including clusters whose luminosities could not be found as described in Section 3.3. As a result, we speculate this could be a reason for the difference in the intercept β values found in Table 4.2. Additionally from Table 4.2, we note the intrinsic scatters from the SDSS DR8 and DES Y3 samples fall within range of each other while our intercept value disagree significantly. Plots of the r_{2500} L_X-λ

relations can be found in Figure 4.3 and Figure 4.4. For a summary of the model parameters see Table 4.2.

Catalog	Relation	Redshift Range	α	β	σ_{intr}	Figure
DES Y3	L_X-λ	0.10< z <0.95	1.15±0.14	0.64±0.07	0.91±0.05	4.3
SDSS DR8	L_X-λ	all redshift	1.37±0.08	-0.08±0.05	0.84±0.04	4.4 (a)
SDSS DR8	L_X-λ	0.1< z <0.35	1.11±0.16	0.02±0.09	0.99±0.06	4.4 (b)

Table 4.2: Here we present fit parameters to the scaling relation ln(y)=α ln($\frac{\lambda}{\lambda_{piv}}$) + β, where y is the L_X observable normalized by E(z) and has units of 10^{44} ergs/s. Our results are compared to those of Hollowood et al. (2018).

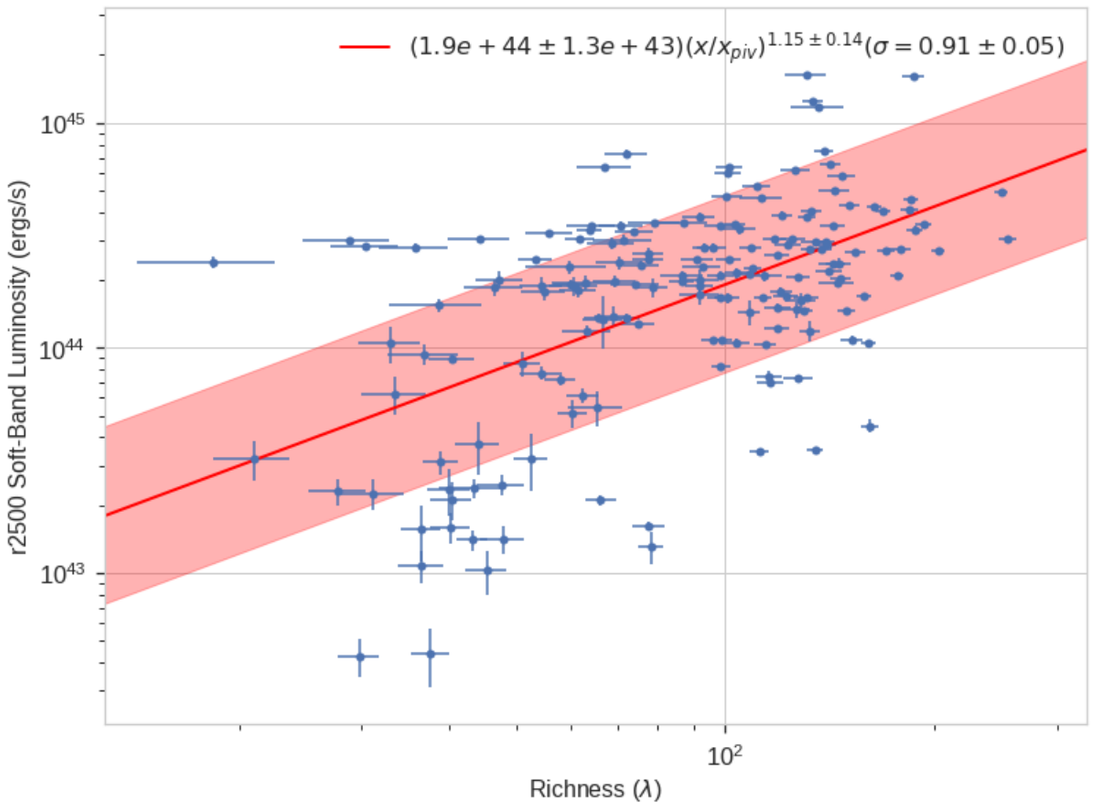

Figure 4.3: An output graph of the $r_{2500}L_X$ - λ regression as derived by CluStR. The red translucent bar indicates the intrinsic scatter about the regression line. Here 'x' in our case refers to the richness λ input. The 'x_{piv}' refers to the pivot point calculated as the median of λ, producing a λ_{piv} = 98. Luminosities are normalized using the Hubble parameter E(z) as a function of redshift. The above relations are for soft-band luminosities.

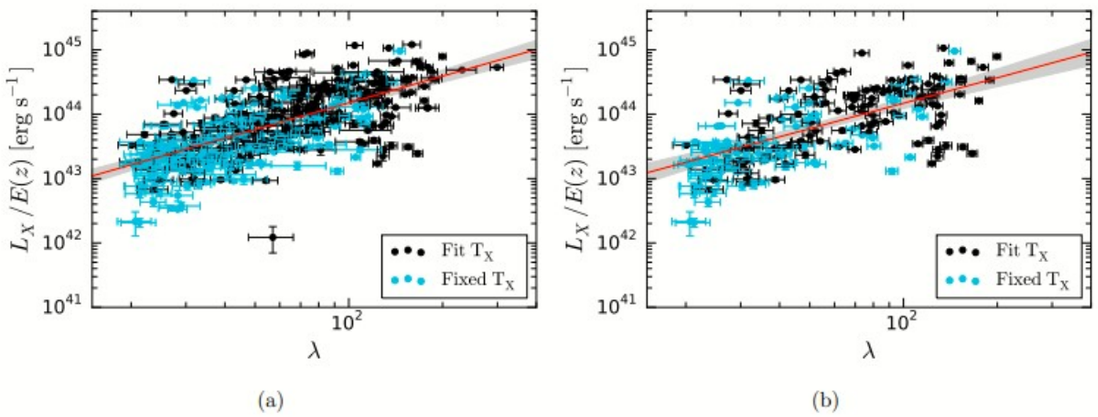

Figure 4.4: (a) r_{2500} L_X-λ scaling relation derived from SDSS DR8 cluster sample (Hollowood et al., 2018) which includes clusters of all redshifts and has no upper limits. (b) Similarly, these are clusters of redshift $0.1 < z < 0.35$. The grey translucent bar indicates the 1σ uncertainties. The red line represents the regression line whose parameters are given in Table 4.2. Black points are clusters that had their L_X fit along with T_X. The cyan points are clusters whose L_X were calculated from an initial assumed T_X as described in section 3.3. This figure was taken from Hollowood et al. (2018).

5

Summary

In this thesis, we summarize the data process from the initial DES cluster catalog to the application of MATCha responsible for providing X-ray imaging analysis for clusters that fall within the Chandra archival data. We then introduced CluStR as a fitting algorithm for studying the scaling relations between $L_X - \lambda$ and $T_X - \lambda$. In this work, we present fits to the scaling relations between X-ray temperature and optical richness along with X-ray luminosity and optical richness for clusters in the DES Y3 redMaPPer catalog. We find an r_{2500} T_X-λ scaling relation of $\ln(E(z)^{-2/3} k_B T_{X,r2500}) = (0.38 \pm 0.06) \ln(\frac{\lambda}{98}) + 1.92 \pm 0.02$ results for 167 'detected' clusters with an intrinsic scatter $\sigma_{intr} = 0.28 \pm 0.02$ and an r_{2500} L_X-λ scaling relation of $\ln(\frac{L_{X,r2500}}{E(z)10^{44}}) = (1.19 \pm 0.14) \ln(\frac{\lambda}{98}) + 0.64 \pm 0.07$ results for 167 'detected' clusters with an intrinsic scatter $\sigma_{intr} = 0.89 \pm 0.05$. The scatter and slope of these relations are consistent with previous studies of lower redshift cluster samples from the Sloan Digital Sky Survey. These measurements will assist in the work toward deriving cosmological constraints using DES clusters by giving a constraint on the intrinsic scatter of optical richness with mass. Similar X-ray follow-ups using redMapper and MATCha will likely extent to larger data sets like the full Dark Energy Survey Y6 catalog and into the upcoming **L**arge **S**ynoptic **S**ky **T**elescope (LSST) survey. Thus, we expect to see the application of CluStR to also extend into the full DES Y6 catalog and LSST survey analysis.

Bibliography

A. Kravtsov and S. Borgani. Formation of galaxy clusters. *Annual Review of Astronomy and Astrophysics*, 50:353–409, Sep 2012. doi: 0066-4146, 1545-4282. URL http://arxiv.org/abs/1205.5556.

T. M. C. Abbott, F. B. Abdalla, S. Avila, M. Banerji, E. Baxter, K. Bechtol, M. R. Becker, and et al. Dark Energy Survey Year 1 Results: Constraints on Extended Cosmological Models from Galaxy Clustering and Weak Lensing. *Physical Review D*, 99:123505, 2019. doi: 10.1103/PhysRevD.99.123505. URL http://dx.doi.org/10.1002/andp.19053221004.

S. W. Allen, A. E. Evrard, and A. B. Mantz. Cosmological Parameters from Observations of Galaxy Clusters. *Annual Review of Astronomy and Astrophysics*, 49:409–470, Sep 2011. doi: 10.1146/annurev-astro-081710-102514. URL http://arxiv.org/abs/1103.4829.

B. C. Kelly. Some Aspects of Measurement Error in Linear Regression of Astronomical Data. *The Astrophysical Journal*, 665:1489–1506, Oct 2007. doi: 10.1086/519947. URL http://arxiv.org/abs/0705.2774.

H. Böhringer and N. Werner. X-ray Spectroscopy of Galaxy Clusters: Studying Astrophysical Processes in the Largest Celestial Laboratories. *The Astronomy and Astrophysics Review*, 18:127–196, 2010. doi: 10.1007/s00159-009-0023-3. URL http://link.springer.com/10.1007/s00159-009-0023-3.

D. G. Gilbank and M. D. Gladders and H. K. C. Yee and B. C. Hsieh. The Red-sequence Cluster Survey-2 (RCS-2): survey details and photometric catalog con-

struction. *The Astrophysical Journal*, 141:94, Mar 2011. doi: 10.1088/0004-6256/141/3/94. URL http://arxiv.org/abs/1012.3470.

E. F. Bell and C. Wolf and K. Meisenheimer and H. Rix and A. Borch and S. Dye and M. Kleinheinrich and L. Wisotzki and D. H. McIntosh. Nearly 5000 Distant Early-Type Galaxies in COMBO-17: a Red Sequence and its Evolution since z 1. *The Atrophysical Journal*, 608:752–767, Jun 2004. doi: 10.1086/420778. URL http://arxiv.org/abs/astro-ph/0303394.

B. Flaugher, H. T. Diehl, K. Honscheid, T. M. C. Abbott, O. Alvarez, R. Angstadt, J. T. Annis, M. Antonik, O. Ballester, L. Beaufore, G. M. Bernstein, R. A. Bernstein, B. Bigelow, M. Bonati, D. Boprie, D. Brooks, E. J. Buckley-Geer, J. Campa, L. Cardiel-Sas, F. J. Castand er, J. Castilla, H. Cease, J. M. Cela-Ruiz, S. Chappa, E. Chi, C. Cooper, L. N. da Costa, E. Dede, G. Derylo, D. L. DePoy, J. de Vicente, P. Doel, A. Drlica-Wagner, J. Eiting, A. E. Elliott, J. Emes, J. Estrada, A. Fausti Neto, D. A. Finley, R. Flores, J. Frieman, D. Gerdes, M. D. Gladders, B. Gregory, G. R. Gutierrez, J. Hao, S. E. Holland, S. Holm, D. Huffman, C. Jackson, D. J. James, M. Jonas, A. Karcher, I. Karliner, S. Kent, R. Kessler, M. Kozlovsky, R. G. Kron, D. Kubik, K. Kuehn, S. Kuhlmann, K. Kuk, O. Lahav, A. Lathrop, J. Lee, M. E. Levi, P. Lewis, T. S. Li, I. Mand richenko, J. L. Marshall, G. Martinez, K. W. Merritt, R. Miquel, F. Muñoz, E. H. Neilsen, R. C. Nichol, B. Nord, R. Ogando, J. Olsen, N. Palaio, K. Patton, J. Peoples, A. A. Plazas, J. Rauch, K. Reil, J. P. Rheault, N. A. Roe, H. Rogers, A. Roodman, E. Sanchez, V. Scarpine, R. H. Schindler, R. Schmidt, R. Schmitt, M. Schubnell, K. Schultz, P. Schurter, L. Scott, S. Serrano, T. M. Shaw, R. C. Smith, M. Soares-Santos, A. Stefanik, W. Stuermer, E. Suchyta, A. Sypniewski, G. Tarle, J. Thaler, R. Tighe, C. Tran, D. Tucker, A. R. Walker, G. Wang, M. Watson, C. Weaverdyck, W. Wester, R. Woods, B. Yanny, and DES Collaboration. The Dark Energy Camera. *The Astrophysical Journal*, 150:150, Nov. 2015. doi: 10.1088/0004-6256/150/5/150. URL https://ui.adsabs.harvard.edu/abs/2015AJ....150..150F.

J. Frieman, M. Turner, and D. Huterer. Dark Energy and the Accelerating Universe. *Annual Review of Astronomy and Astrophysics*, 46: 385–432, 2008. doi: 10.1146/annurev.astro.46.060407.145243. URL http://arxiv.org/abs/0803.0982.

A. Gelman, J. B. Carlin, H. S. Stern, D. B. Dunson, A. Vehtari, and D. B. Rubin. *Bayesian Data Analysis*. Chapman Hall/CRC, 3 edition, Nov 2013. ISBN 9781439898222.

D. L. Hollowood, T. Jeltema, X. Chen, A. Farahi, A. Evrard, S. Everett, E. Rozo, E. Rykoff, R. Bernstein, A. Bermeo, L. Eiger, P. Giles, H. Israel, R. Michel, R. Noorali, K. Romer, P. Rooney, and M. Splettstoesser. Chandra Follow-up of the SDSS DR8 redMaPPer Catalog Using the MATCha Pipeline. *The Astrophysical Journal Supplement Series*, 244:22, 2019. doi: 10.3847/1538-4365/ab3d27. URL http://arxiv.org/abs/1808.06637.

M. C. Weisskopf and H. D. Tananbaum and L. P. Van Speybroeck and S. L. O'Dell. Chandra X-ray Observatory (CXO): Overview. 4012:2–16, July 2000. doi: 10.1117/12.391545. URL https://ui.adsabs.harvard.edu/abs/2000SPIE.4012....2W.

M. D. Gladders and H. K. C. Yee. The Red-Sequence Cluster Survey. I. The Survey and Cluster Catalogs for Patches RCS 0926+37 and RCS 1327+29. *The Astrophysical Journal Supplement Series*, 157:1–29, Mar 2005. doi: 10.1086/427327. URL http://adsabs.harvard.edu/abs/2005ApJS..157....1G.

W. H. Press, S. A. Teukolsky, W. T. Vetterling, and B. P. Flannery. *Numerical Recipes The Art of Scientific Computing*. Cambridge University Press, 3 edition, Sep 2007. ISBN 9780521880688.

E. Rozo, E. S. Rykoff, B. P. Koester, T. McKay, J. Hao, A. Evrard, R. H. Wechsler, S. Hansen, E. Sheldon, D. Johnston, M. Becker, J. Annis, L. Bleem, and R. Scranton. IMPROVEMENT OF THE RICHNESS ESTIMATES OF maxBCG CLUSTERS. *The Astrophysical Jour-*

nal, 703:601–613, 2009. doi: 10.1088/0004-637X/703/1/601. URL https://doi.org/10.1088%2F0004-637x%2F703%2F1%2F601.

E. S. Rykoff, B. P. Koester, E. Rozo, J. Anne, A. E. Evrard, S. M. Hansen, J. Hao, D. E. Johnston, T. A. McKay, and R. H. Wechsler. Robust Optical Richness Estimation with Reduced Scatter. *The Astrophysical Journal*, 746:178, Feb. 2012. doi: 10.1088/0004-637X/746/2/178. URL http://adsabs.harvard.edu/abs/2012ApJ...746..178R.

E. S. Rykoff, E. Rozo, M. T. Busha, C. E. Cunha, A. Finoguenov, A. Evrard, J. Hao, B. P. Koester, A. Leauthaud, B. Nord, M. Pierre, R. Reddick, T. Sadibekova, E. S. Sheldon, and R. H. Wechsler. redMaPPer. I. Algorithm and SDSS DR8 Catalog. , 785:104, Apr. 2014. doi: 10.1088/0004-637X/785/2/104.

C. L. Sarazin. *X-RAY EMISSIONS FROM CLUSTERS OF GALAXIES*. 1988. URL https://ui.adsabs.harvard.edu/abs/1988xrec.book.....S.

The-Dark-Energy-Survey-Collaboration. The Dark Energy Survey. 2005. URL http://arxiv.org/abs/astro-ph/0510346.

G. M. Voit. Tracing cosmic evolution with clusters of galaxies. *Reviews of Modern Physics*, 77:207–258, 2004. doi: 10.1103/RevModPhys.77.207. URL http://arxiv.org/abs/astro-ph/0410173.

H. Wu, E. Rozo, and R. H. Wechsler. Annealing a Follow-up Program: Improvement of the Dark Energy Figure of Merit for Optical Galaxy Cluster Surveys. *The Astrophysical Journal*, 713:1207–1218, Apr 2010. doi: 10.1088/0004-637X/713/2/1207. URL http://adsabs.harvard.edu/abs/2010ApJ...713.1207W.

UNIVERSITY of CALIFORNIA
SANTA CRUZ

SCALING RELATIONS FOR THE DARK ENERGY SURVEY YEAR THREE CATALOG

A thesis submitted in partial satisfaction of the
requirements for the degree of

BACHELOR OF SCIENCE

in

ASTROPHYSICS

by

Paige Kelly

February 6 2021

Abstract

SCALING RELATIONS FOR THE DARK ENERGY SURVEY YEAR THREE CATALOG

by

Paige Kelly

Galaxy clusters are excellent probes of dark energy in the universe due to how large they are. Their mass throughout time can give insight to the evolution of dark energy. The mass of galaxy clusters can not be determined directly, but the mass is related to other observables. For this thesis I created scaling relations using information from the Dark Energy Survey Year Three (DES Y3) data set between the X-ray observable temperature (T_x) and richness (λ) of galaxy clusters that can be used to understand the evolution of the universe and the affect dark energy had on it. I found the relation with no restriction on redshift for an r_{2500} aperture to be $\ln(E(z)^{\frac{-2}{3}} k_b T_{xr_{2500}}) = 0.54 \pm 0.06 \ln(\frac{\lambda}{\lambda piv}) + 2.02 \pm .02$ with the standard-deviation-of-intrinsic-scatter valued to be 0.24 ± 0.02. I also ran a fit for the redshift range $0.2 < z < 0.65$ and found the relation to be $\ln(E(z)^{\frac{-2}{3}} k_b T_{xr_{2500}}) = 0.54 \pm 0.07 \ln(\frac{\lambda}{\lambda piv}) + 2.09 \pm .03$ with a standard-deviation-of-intrinsic-scatter found to be 0.26 ± 0.02. The fits I found agree well with past results with all aspects except the intercept value.

Contents

List of Figures

List of Tables

To Bun

Acknowledgements

I would like to start by thanking Tesla Jeltema for her consistent guidance throughout my time at the University of California, Santa Cruz. She has inspired me since the first class I took after transferring up until finalizing this thesis. I feel so incredibly lucky to have been in her research group filled with kind, caring, hardworking, and intelligent people. The opportunity she has given me is everything I wanted and more in my college experience. It has been an absolute joy going from understanding almost nothing said in my first research meeting to where I am now. I am so thankful for the supportive and productive research environment Tesla Jeltema has created. Tesla, I cannot thank you enough. You have made an impact on my life that I will forever be grateful for.

Much of the work provided in this thesis was explained to me in countless meetings with Spencer Everett. Spencer, thank you for all of the hours you spent helping me reach this point and for always making me feel like no question is a bad question. Your passion for physics is truly inspiring.

1

Introduction

Based on many cosmological observations, the current standard model of the universe, until proven otherwise, is called the concordance model. Under this model, the universe is understood to be flat with an accelerating expansion. The acceleration of the universe can be observed by using type Ia supernovae as standard candles (Riess, 1998; Perlmutter, 1999). Type Ia supernovae have a consistent luminosity. Under observation, high redshift Type Ia supernovae were appearing fainter than they should be if the universe were not accelerating, leading to the discovery of the accelerating universe (Riess, 1998; Perlmutter, 1999). Two separate teams of astronomers including Adam Riess, Saul Perlmutter, and Brian Schmidt independently made these initial discoveries in the 1990's. The accelerating nature of the universe required something else that was not the known ordinary matter, dark matter, or light. Without another component, the universe's expansion would instead be slowing down. Current observations are consistent with the missing information being a cosmological constant with a negative pressure which represents dark energy, though it is possible it could be an energy density which changes in time rather

than being constant (Riess, 1998; Perlmutter, 1999). Regardless, dark energy is causing the accelerating expansion of the universe.

The effect of dark energy on the expansion history of the universe changes the growth of structure and can be probed by looking at structure formation over time. In particular, clusters of galaxies are effective to use due to how large these cosmological structures are. Looking at further away clusters can give insight into galaxy clusters from earlier on in the formation of the universe due to the time it takes the light to reach observers. They can be compared to the density of closer clusters to understand their formation as well as the role dark energy had in their formation. This can provide insight into the density of dark energy throughout time and if it is constant as currently believed.

Galaxy clusters are produced by gravitational in-fall. Essentially, a smaller object, that is denser than the surrounding area has gravity that pulls more objects in, which are eventually grouped to form into galaxies whose gravity pulls in more galaxies—these galaxies that have collected are called galaxy clusters. They are roughly 10^{15} times the mass of the sun and have decoupled from the expansion of the universe (Voit, 2005). In addition to galaxies, galaxy clusters contain hot gas and dark matter (Voit, 2005). The dark matter creates a halo filling and surrounding the cluster, with the hot gas and clusters inside of the halo. Most of the mass in a galaxy cluster is from the hot gas and dark matter (Voit, 2005). Dark Matter is a form of matter that has not been detected directly. It is non-interacting, but its gravitational effects can be seen. Our current theories of gravity show there is not enough baryonic matter in the universe to prevent galactic structures, like galaxies and galaxy clusters, from moving away from each other or for them to have formed to begin with. Dark matter is non-baryonic and accounts for this "missing" matter in the universe

that helped with the formation of structures like galaxy clusters (Voit, 2005). Clusters form through gravity during the accelerated expansion of the universe, meaning the formation of galaxy clusters is sensitive to dark energy as well.

The Dark Energy Survey provided the large samples of clusters required for this project. The goal of the Dark Energy Survey (DES) is to understand the nature of dark energy. To meet this goal, over 400 scientists from around the world are collaborating to map and then study galaxies, supernovae, and patterns of cosmic structure (Lahav et al., 2020). 5000 degrees of the sky has been analyzed and information on roughly 300 million galaxies has been found using the Dark Energy Camera (DECam) mounted on the Blanco 4m telescope located at the Cerro Tololo Interamerican observatory in Chile (Flaugher, 2015). The telescope was built in the 1970's and the DECam was added in 2012 after four years of assembly. DES uses five filters with a diameter of 62cm—the sky is imaged by each of these which range between 400nm to 1080nm (Flaugher, 2015). The camera holds 74 CCDs, and the specific ones used by DES were designed by scientists at the Lawrence Berkeley National Laboratory (Flaugher, 2015). They were intended to detect distant galaxies, which is easier to do with thicker CCDs because the likelihood of detecting longer wavelengths increases with thickness, so they were designed ten times thicker than they typically are (Flaugher, 2015). It is still true that it is more difficult to detect distant galaxies. The galaxies being analyzed in this thesis are from the DES year three (Y3) data set. These galaxies are grouped into clusters and can be further analyzed to eventually determine the masses of galaxy clusters.

The galaxy cluster mass function refers to the number density of clusters as a function of mass. The way dark energy is probed is by looking at the mass function and its

evolution–this means we need mass. Lensing can directly determine the mass of a galaxy cluster, but this method is not practical while studying large quantities of galaxy clusters . Instead, we can calibrate these clusters using X-ray follow up. It is an excellent observable-based method of studying dark energy in the universe (Farahi et al., 2019; Hollowood, 2019; Zhang, 2019). There are various observables that correlate with mass, but they all have scatter we need to understand (Wu, 2010). These observables include the temperature, luminosity, and richness of the galaxy clusters (Hollowood, 2019). A linear regression between the richness of a cluster to an X-ray observable can provide insight to the evolution of the universe which we can use to understand the nature of dark energy. Richness is an observable used by DES that refers to the amount of galaxies in a given cluster. I created a code called CluStR with Jose Jovel mentored by Spencer Everett that can create these relations.

The Background of this thesis will detail the two programs that are implemented before CluStR is used. The CluStR section will describe the purpose and functionality of the CluStR code. The results section will contain the plots made by CluStR along with their respective scaling relations with information about what can be done with them. Finally, the results section will summarize my findings and discuss the possibilities for the future of CluStR.

2

Background

2.1 RedMaPPer

When mapping galaxies based on their color and magnitude two groups become clear. One of these groups, the 'blue cloud,' contains blue galaxies with a large color dispersion. The other contains red galaxies that have a tight relationship with a small range of colors that belong to the 'red sequence.' Most galaxies fit in either the red sequence or the blue cloud. Galaxies in the red sequence are early-type galaxies that tend to cluster together (Eales et al., 2018). In log space, a linear correlation can be seen when mapping the X-ray observables luminosity (L_x) or temperature (T_x) of a set of galaxy clusters to the number of galaxies in each cluster, which is known as richness (λ). From this, a mass relation can be determined.

The galaxies identified by the Dark Energy Survey from year three (DES Y3) must be run through an algorithm that identifies clusters by their red sequence and their properties. The red-sequence Matched-filter Probabilistic Percolation (redMaPPer) cluster

finder identifies these clusters by taking galaxies of known spectroscopic redshifts and then finds groups of galaxies with similar color to model the red sequence (Rykoff, 2014). The red sequence model is then applied to the galaxies from DES Y3 and galaxy clusters can be determined along with a probability of the richness of the cluster. The probabilistic centers of the clusters are found by iterating through possible central galaxies and removing the less likely centrals. The five galaxies that are most likely to be the centers are kept (Rykoff, 2016). A fraction of the galaxy clusters identified by redMaPPer can be analyzed further by being compared to *Chandra* X-ray observations (Hollowood, 2019).

2.2 MATCha

Further analysis can be done by using the Mass Analysis Tool for *Chandra* (MATCha) pipeline. MATCha takes in a list of sky coordinates and redshifts of the clusters found using redMaPPer and runs them through several *Chandra* Interactive Analysis of Observations (CIAO) tools (Hollowood, 2019). The first tool called *find_chandra_obsid* determines which clusters from the data are also covered by *Chandra* data. *Chandra* has not observed the whole sky, so only clusters that have been observed by *Chandra* are analyzed. The *Chandra* instrument is sensitive to a wide energy range, so we limit the energy range to the band where *Chandra* is most sensitive and best calibrated (Fruscione, 2006). Unlike optical, we do not use filters. In X-ray we can estimate the energy of each individual photon and then pick the ones we want to use. The data covered by *Chandra* is then downloaded and further refined with the CIAO tool *chandra_repo*. Time periods with high particle background are called flares. MATCha removes the flares with another CIAO tool called *deflare*. Images and exposure maps can then be made. Following these steps, point sources are identified

and they are removed using the tool *wavedetect* (Fruscione, 2006).

The *Chandra* X-ray observatory, which is a NASA facility, has an instrument called the Advanced CCD Imaging Spectrometer (ACIS) that is composed of 10 CCDs. It was created by the Massachusetts Institute of Technology alongside the Pennsylvania State University. Four of these chips are front illuminated and are referred to as the ACIS-I array. Four of the remaining chips are also front illuminated, with the other two being back illuminated. They are arranged in a row and make up the ACIS-S array (Plucinsky, 2018). Due to these differences, ACIS-S and ACIS-I have inconsistent instrument response. Response files are based on the efficiency of the detection of photons at different energies, and they account for the different responses throughout the CCDs (Hollowood, 2019). Because of the inconsistencies, observations on the ACIS-S array are cleaned one chip at a time, and ACIS-I observations can be cleaned as a group since the ACIS-I array does not have major differences between each chip (Hollowood, 2019). Clusters are then ready to be analyzed one at a time by MATCha (Hollowood, 2019).

In the individual cluster analysis, the goal is to fit an X-ray temperature (T_x), an X-ray luminosity (L_x), as well as X-ray centroids which are computed using the CIAO tool *dmstat* (Hollowood, 2019). Due to the unique responses of each CCD, specifically for the ACIS-S array, the source and background regions are constrained to be on the CCD of the centroid. The source and background for the ACIS-I must lie on the array due to the similarity between the CCDs (Hollowood, 2019). Through an iterative process, first a centroid is found within a 500kpc radius with the starting point being the redMaPPer center. The centroid is then updated to the new centroid, and the process is repeated with the updated centroid. This process allows there to be 500kpc from the redMapper center

and the final centroid found by MATCha. If the new center is found to be within 15kpc of the previous center, then the iteration stops, if this does not occur before 20 iterations are complete, the cluster is considered undetected. A cluster is also considered undetected if the signal-to-noise ratio in the final 500 kpc region is less than 5. For those clusters marked undetected, MATCha will fit an upper limit for L_x. MATCha will then try to fit T_x and L_x for the detected clusters (Hollowood, 2019).

For the detected clusters, the background is determined as an annulus with the inner radius being 700kpc and the outer being 1000kpc, this is done with the tool *specextract* (Fruscione, 2006). MATCha can then find a background-subtracted spectrum for the 500kpc radius which is used to attempt to fit T_x and L_x values using the tool *XSPEC* (Fruscione, 2006). If the fit can be completed, using the value determined for T_x, a radius around each galaxy cluster halo is fit at the point the average density is 2500 times the cosmological critical density. This radius is referred to as r_{2500}. A new centroid, T_x, and L_x is then determined using the r_{2500} radius. The process is the same as before, and if the new centroid is not found within 20 iterations, it is aborted. Using the new temperature, a new value for r_{2500} is calculated, if it is within 1σ of the last value for r_{2500} then the value for r_{2500} is considered to have converged. MATCha then moves on to the radius at 500 times the cosmological critical density, or r_{500}. The process for this is identical, except the most recently determined centroid is used for the new initial centroid (Hollowood, 2019). After running MATCha, we now have galaxy clusters that have various values for T_x and L_x that can eventually be used in regression analysis.

After the automated MATCha analysis we examine the output. The galaxy clusters must be manually examined by members of my research team to determine potential

flags. The flags will label issues such as a cluster too close to the chip edge or any interesting features such as a cluster that is merging (Hollowood, 2019). A catalog is then created with these flags identified as well as the data on each cluster determined by MATCha and redMaPPer. Some of the flags must be cut from the catalog before a linear regression can be determined. Details on specific flags and cuts can be found in section 3.2.3. Linear regressions can then be determined between T_x or L_x and richness.

3

CluStR

3.1 Scaling Relations

The complete catalog of galaxy clusters is then ready for regression analysis. The model used must produce a relationship between the X-ray observable T_x or L_x and λ while accounting for intrinsic scatter as well as error. The error analysis must account for correlated measurement, censored data, and heteroscedastic errors (Hollowood, 2019). Brandon Kelly produced a Bayesian method that meets these requirements. The program is called linmix. Determining the parameters in the linear regression directly is not appropriate as it is a too intensive process. Instead, the linear relationship is determined through a likelihood function (Kelly, 2007). A Gibbs sampler is used to do this. First, the Gibbs sampler creates additional data points based on the known data points. This process is known as data augmentation (Kelly, 2007). The sampler then simulates the regression parameters followed by the mixture parameters. The parameters are saved, and the process is iterated with the past values being accounted for. This iteration is done many times creating a Markov Chain

which eventually converges. Histogram estimates based on the random draws can be used to estimate the posterior distribution meaning regression parameters with their relevant errors can be identified (Kelly, 2007).

Clusters with the same underlying properties can have a variety of observed properties. For example, not all clusters with a given mass will have the same richness or luminosity. The regression only gives the average relation and clusters will scatter around this relation even if there is no error in the observables. This scatter is called intrinsic scatter and Brandon Kelly's program accounts for this. The output of linmix is the slope and intercept of the line along with the value of intrinsic scatter. The output plot for the posterior distribution can be found in the Results section in Figure 4.2, and this shows how the values for slope, intercept, and intrinsic scatter were reached along with the estimates for their errors.

3.2 CluStR Code

A code is required to first download the detected red sequence clusters along with their observables, create cuts on nonviable clusters, then create a linear regression using Brandon Kelly's program linmix, and lastly the results from linmix are used to make a plot. I wrote a code called CluStR that does this with Jose Jovel, mentored by Spencer Everett. The new code was written so that it could be easily used to serve other purposes in the future—it was softcoded. Currently it is used in conjunction with the previously mentioned program linmix, but since it is softcoded, other programs could be used instead. The user has more options; for example, they can set their own parameters before they run the code. The following section further outlines the details of the code along with how to use it.

3.2.1 Inputs

When running the code, inputs are required. The first input is the chosen catalog of galaxy clusters. As previously mentioned, data from DES Y3 was used for our purposes and run through redMaPPer and MATCha then manually examined to create the catalog being used. The second input is the choice for the x-axis. The options can be adjusted depending on the catalog being used, but for our catalog they are set to be from the column names which include: 500_kiloparsecs_band_lumin, r2500_band_lumin, r500_band_lumin, r500_core_cropped_band_lumin, 500_kiloparsecs_temperature, r2500_temperature, r500_tempurature, r500_core_cropped_temperature. For the column names, r2500_temperature and r2500_band_lumin for example refer to the temperature and luminosity respectively inside r_{2500} regions as determined by MATCha. The shorthand versions of these are what are entered into the terminal for simplicity, they are as follows: l500kpc, lr2500, lr500, lr500cc, t500kpc, tr2500, tr500, tr500cc, and lambda. Shorthand versions can be changed by the user. The third input is the y-axis. The fourth input is the configuration (config) file.

The config file we created that contains parameters for the CluStR program. For our purposes, some of the settings are intended to remain unchanged, while others are meant to be changed by the user as needed. The value in having a file that has a wide range of parameters programmable by the user is to make the code more versatile. Different catalogs with different column names can be set, other programs beside linmix can be used, the range option can be adjusted, the cutoff option can be changed, the Boolean flags can be chosen, and there are options regarding the plots to be made and which ones to save. To remove data with a given Boolean flag, set the chosen flag and then set it to 'True.' For the 'Cutoff_Flag' section in the config file, set the first option to 'True,' then set the cutoff to the integer value

desired and set the cutoff type to ‘above,’ or ‘below.’ For the flag option ‘Range_Flag’, set the third option to ‘True’ to activate it, then set the minimum and maximum range values and set the range type to ‘inside’ or ‘outside.’ To have a plot be made and saved, the user needs to set the plots they want to ‘True.’

The fifth input requirement is the plotting library. The plotting file used for this project was made by Spencer Everett in 2017 with minor edits done more recently. There are several settings in the config file that dictate how this library will run and what plots will be made as previously mentioned. Currently the code can produce scatter, residuals, chains, and corner plots. Examples of the scatter plots can be found in the results section.

3.2.2 How CluStR Works

In the CluStR code itself, after collecting all the appropriate inputs and loading and opening the needed catalog, config file, and plotting file, cuts are made on the unwanted data in the function titled ‘create_cuts.’ All flags that are determined by what the user sets in the config files are removed from the data by this function. The cuts I made for this project will be explained in section 3.2.3. There are three types of possible flags for our purposes, they can be Boolean, cutoff, or range. The Boolean flags refer to the ‘True’ or ‘False’ options. Range flags remove data inside or outside the range setting which is a redshift range for our purposes, and cutoff flags removes data above or below the cutoff. The option of ‘inside’ or ‘outside’ for the range or ‘above’ or ‘below’ for the cutoff is set in the config file as previously mentioned. The code loops through the possible flags set in the config file under the Boolean type flags and identifies which flags are set to ‘True.’ The process is then repeated for data not ‘inside’ or ‘outside’ the redshift range. It is repeated

once more for data 'above' or 'below' the cutoff. It then loops through the catalog and finds any data that has any of these flags. The user is notified how many clusters have each given flag. The rows that have no flags in them, which we called 'good_rows', are now known and everything else is removed from the x and y data. The x and y errors, 'x_err' and 'y_err' respectively, can then also be determined. The data is scaled using the 'scale_data' function–it is put into log space, so the fit is linear and simpler to analyze. Linmix is then run with the inputs being x, y, x_err, and y_err all in log space, to determine an equation for a line appropriate to the data along with a value of sigma, the scatter. The final step is to create a plot using the good data, the results from linmix, and the plotting file uploaded by the user. These plots can then be further analyzed.

3.2.3 Flags

I removed data that contained the Boolean flags masked, bad_mode, edge_r2500, overlap_r2500, edge_bkgd, overlap_bkgd, and overlap_r500. In the config file each of these have '_bool_type' appended at the end. Clusters that are marked 'masked,' are clusters that are not actually a redmapper cluster but were falsely identified as one by MATCha because there is a bright X-ray cluster along the same line of sight to the redmapper cluster. We want clusters to be detected by *Chandra* in an imaging mode, and those that are not are flagged as 'bad_mode.' Clusters that were not entirely on the CCD are flagged as 'edge_r2500.' For the flag 'overlap_r2500,' the correct cluster was analyzed, but a nearby cluster is contaminating the observation. The second cluster was within the r_{2500} aperture of the analyzed cluster. Removing the following two flags is more conservative. The flag 'overlap_bkgd' refers to clusters that are overlapping, but the second cluster is within the

background region of the analyzed cluster. The flag 'overlap_r500' is the same as the flag 'overlap_r2500,' except the nearby cluster is within the r_{500} aperture. In addition to Boolean flag cuts, I also made cuts on data that had a signal to noise ratio higher than nine. This is done using the cutoff option and setting the cutoff to 9.0 and setting the cutoff type to below. I ran two fits, one with a redshift range from $0.0 < z < 1.0$ and one with a more conservative range from $0.2 < z < 0.65$. With these cuts made, out of the 1092 galaxy clusters in the catalog, only 137 galaxy clusters remained for the larger redshift range and 98 remained for the more conservative range. The remaining galaxy clusters are used in the analysis.

4

Results

The data used for the fit I produced was from DES Y3. The program redMaPPer was used to group the galaxies into clusters and then identify each cluster's redshift before MATCha finds the temperatures and luminosities for each galaxy cluster. The program CluStR can then be run with the proper inputs. The x-axis for our purposes is chosen to be lambda, the richness. I chose tr2500 for the y-axis. The X-ray temperature within an r_{2500} region was chosen because temperature is a better measure of cluster mass than the luminosity because it has a lower intrinsic scatter. With these options, along with the libraries included on the CluStR repository, the code can be run. The flags used by CluStR to remove problematic clusters for this fit included 39 clusters with the flag masked, 9 flagged bad_mode, 41 flagged edge_r2500, 7 flagged overlap_r2500, 52 flagged edge_bkgd, 27 flagged overlap_bkgd, and 15 clusters were flagged overlap_r500. In addition to the Boolean flags identified, 840 clusters were cut due to their signal to noise ratio being below 9. I am running two fits, the first is without a redshift cut and the second has a cut based on redshift. Both fits have the same cuts besides the redshift. I am doing both fits to

discover if the results are consistent. It may be beneficial to cut the lower redshift clusters because the galaxy clusters with lower redshifts were not the primary focus when data was being taken. A filter that is blue enough was not used. As previously mentioned, the thickness of the CCDs was intended for detecting larger redshifts. In addition, richness is less accurate at higher redshift due to the difficulty in detecting fainter galaxies. To account for this, redMaPPer makes estimates for the likely amount of galaxies in the cluster. These things lead to higher uncertainty in the lower and higher redshifts. Though this is true, in past results, setting the redshift range to these more conservative values has not shown a significant difference in results (Hollowood, 2019). For my fits, the redshift range $0.0 < z < 1.0$ no clusters are cut due to redshift. After all cuts were made under this redshift range, 272 of the remaining clusters did not have a value for the X-ray temperature within an r_{2500} region so those were also cut. For the redshift range $0.2 < z < 0.65$, 667 galaxy clusters are cut due to the redshift. After the final cuts, 194 clusters did not have temperature values, so they were removed. Some galaxy clusters have multiple of each flag meaning the total identified flags is larger than the number of cuts made. 137 galaxy clusters out of the initial 1092 clusters remained for the large redshift range and 98 clusters remained for the conservative range after the code was run. The two plots of the T_x-λ scaling relation are displayed in Figure 4.1.

The relations derived by the CluStR code alongside Brandon Kelly's code linmix are in the form $\ln(E(z)^{\frac{-2}{3}} k_b T_{xr_{2500}}) = \alpha \ln(\frac{\lambda}{\lambda piv}) + \beta$ where λ is the richness of the cluster, and λ_{piv} is the pivot point. We chose the pivot point to be the median of the richness data points. The X-ray temperature is normalized by the factor $E(z)^{\frac{-2}{3}} k_b$ where k_b is the Boltzman constant and E(z) is the dimensionless Hubble Parameter. E(z) = H(z)/H where

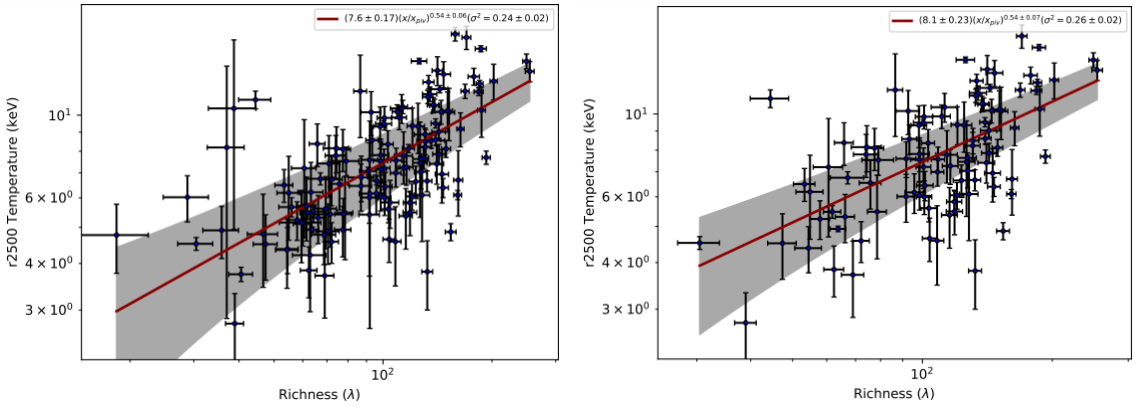

Figure 4.1: The T_x – λ relation for an r_{2500} aperture that has no redshift cut applied is shown on the left. The plot on the right is under the redshift range 0.2 < z < 0.65. The fit for these plots have no significant difference between the intrinsic scatters or the slope, but there is a slight difference in the slope. The shaded region represents the intrinsic scatter of the line.

H is the Hubble constant, which we are accepting to be $70 kms^{-1}Mpc^{-1}$, and H(z) is the Hubble parameter at a given redshift. The results for these fits are summarized in Table 4.1. For the T_x – λ relation for an r_{2500} aperture with the redshift range 0.0 < z < 1.0, we determined the relation

$$ln(E(z)^{\frac{-2}{3}} k_b T_{xr_{2500}}) = 0.54 \pm 0.06 ln(\frac{\lambda}{\lambda piv}) + 2.02 \pm .02 \tag{4.1}$$

The intrinsic scatter and its uncertainty were measured to be $\sigma_{intr} = 0.24 \pm 0.02$ meaning sigma is measured to within 8 percent. Our data has been normalized to our pivots, and for this relation I determined $\lambda_{piv} = 103$. For the T_x – λ relation for an r_{2500} aperture with the redshift range 0.2 < z < 0.65, we determined the relation

$$ln(E(z)^{\frac{-2}{3}} k_b T_{xr_{2500}}) = 0.54 \pm 0.07 ln(\frac{\lambda}{\lambda piv}) + 2.09 \pm .03 \tag{4.2}$$

The standard-deviation-of-intrinsic-scatter was measured to be $\sigma_{intr} = 0.26 \pm 0.02$ meaning sigma is measured to within 8 percent. For this redshift range, I determined $\lambda_{piv} = 117$. The values for sigma and slope for the conservative redshift range have no significant difference

between the values where there are no cuts based on redshift. The intercepts are however not within range, but the values are still close. There are several outliers with large error that were removed with the redshift cut that cause this slight difference in results.

Dataset	Redshift	α	β	σ_{intr}
DES Y3	$0.2 < z < 0.65$	0.54 ± 0.07	$2.09 \pm .03$	0.26 ± 0.02
DES Y3	all	0.54 ± 0.06	$2.02 \pm .02$	0.24 ± 0.02

Table 4.1: $T_x - \lambda$ relations for an r_{2500} aperture determined using DES Y3 data.

Dataset	Redshift Range	α	β	σ_{intr}
DES Y1 (A. Farahi et al., 2019)	$0.2 < z < 0.70$	0.56 ± 0.09	X	0.260 ± 0.032
SDSS (Hollowood et al., 2019)	all	0.54 ± 0.04	1.82 ± 0.02	0.26 ± 0.02
SDSS (Hollowood et al., 2019)	$0.1 < z < 0.35$	0.52 ± 0.05	1.85 ± 0.03	0.27 ± 0.02

Table 4.2: $T_x - \lambda$ relations for an r_{2500} aperture for other samples in different redshifts are displayed.

A. Farahi et al. (2019) produced similar results for DES Y1 under the redshift range $0.2 < z < 0.70$ also using *Chandra* data that are displayed in Table 4.2. This study determined the slope to be 0.56 ± 0.09 and the residual scatter to be 0.260 ± 0.032. The value for intrinsic scatter is closest to the intrinsic scatter determined for our redshift range for $0.2 < z < 0.65$, but both values for intrinsic scatter I determined are within the error range determined by A. Farahi et al. Both values we determined for the slope are also well within the error range determined by A. Farahi et al. They did not directly report their results for the intercept. There was no data for an unrestricted redshift range.

In a separate study conducted by Hollowood, Jeltema, Chen, et al. (2019), similar results were also produced for redMaPPer clusters in the previous SDSS survey which can be seen in Table 4.2. For all redshifts, the slope was determined to be 0.54 ± 0.04 which is the value we determined it to be except we had slightly larger errors. Hollowood, Jeltema,

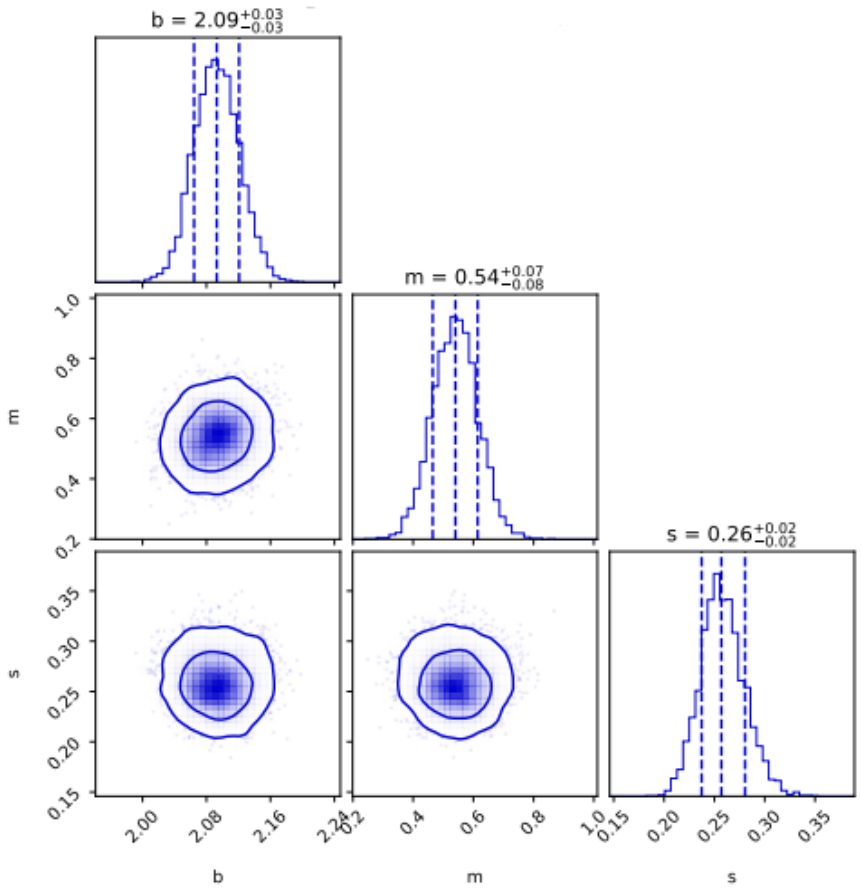

Figure 4.2: This is an example of the posterior distribution for the restricted redshift range. A Markov Chain is simulated that begins a random walk saving each point as it goes along creating the posterior distribution. This means the regression parameters along with their errors can be estimated as displayed. The posterior distribution may not be the same each time it is run since it is a likelihood function based on random draws, but they are very close.

Chen, et al. determined the intercept to be 1.82 ± 0.02. My value for intercept under all redshifts is not within their error. The intrinsic scatter was estimated to be 0.26 ± 0.02 which is within our error. Their study also examined a narrower redshift range than our restricted redshift range where $0.1 < z < 0.35$. The slope was determined to be 0.52 ± 0.05 and our value, though the redshift range is different, is well within the error ranges. The intrinsic scatter was found to be 0.27 ± 0.02 which agrees with my value of intrinsic scatter. They identified the intercept as 1.85 ± 0.03 and my value for intercept is again not within the range. There is a slight disagreement in normalization–the values for richness between the different samples are not exactly the same, which could contribute to the shift in intercept. The data agrees well with my values for the slope and intrinsic scatter, but are slightly different for the intercept values. In the study conducted by Hollowood, Jeltema, Chen, et al., it was concluded that there is no significant difference between the equations of a line for all redshifts and for the redshift range where $0.1 < z < 0.35$. The two equations were within the error range. My two equations were only slightly different due to the intercepts not being within the error range.

5

Summary

For this thesis I created fits for the relationship between cluster observable properties while including their scatter using the program CluStR that I wrote with Jose Jovel to create plots that can be used to understand the density of dark energy throughout time. The code was created with the intention of it being used for other projects in the future. Parameters can be changed by the user to make it more versatile. Before the code is implemented for my purposes, galaxies mapped by DES were grouped into galaxy clusters by redMaPPer which also identified the estimated redshift and richness of each cluster. MATCha is then implemented and galaxies are compared to *Chandra* data to find the X-ray temperatures and luminosities of the clusters. Tesla Jeltema's research team then manually examined the clusters to identify flags. The clusters with the information determined are then put into catalogs so the clusters can be further narrowed down to the appropriate data and fit using the program CluStR. The T_x – λ scaling relation for the r_{2500} region with no cut on redshift was determined to be $\ln(E(z)^{\frac{-2}{3}} k_b T_{xr_{2500}}) = 0.54 \pm 0.06 \ln(\frac{\lambda}{\lambda piv}) + 2.02 \pm .02$ and the standard-deviation-of-intrinsic-scatter was determined to be 0.24 ± 0.02.

In addition, the T_x – λ scaling relation for the redshift range $0.2 < z < 0.65$ was found to be $\ln(E(z)^{\frac{-2}{3}} k_b T_{xr_{2500}}) = 0.54 \pm 0.07 \ln(\frac{\lambda}{\lambda piv}) + 2.09 \pm .03$ and the standard-deviation-of-intrinsic-scatter was determined to be 0.26 ± 0.02. The redshift cut did not change the slope or value of sigma, but it did slightly increase the intercept. Where as in past results there was no significant difference between slope, sigma, or intercept with a change in the redshift range. This minor difference in my fits could be due to several outliers that were cut due to the redshift range.

The program CluStR can be used for a variety of future projects that wish to create a linear regression. Before any more projects are started, minor edits will be made to the program CluStR to make the code more organized and run more quickly. These edits will not change any results. As soon as CluStR has been edited, the code will be used for the DES Y3 X-ray follow up paper which will include both the *Chandra* data described here and XMM data. Fits of L_x versus λ will also be included for this upcoming project.

Bibliography

Eales, S. A., Baes, M., Bourne, N., Bremer, M., Brown, M. J. I., Clark, C., Clements, D., de Vis, P., Driver, S., Dunne, L., Dye, S., Furlanetto, C., Holwerda, B., Ivison, R. J., Kelvin, L. S., Lara-Lopez, M., Leeuw, L., Loveday, J., Maddox, S., Michałowski, M. J., Phillipps, S., Robotham, A., Smith, D., Smith, M., Valiante, E., van der Werf, P., & Wright, A. (2018). The causes of the red sequence, the blue cloud, the green valley, and the green mountain. , 481(1), 1183–1194.

Farahi, A., Chen, X., Evrard, A. E., Hollowood, D. L., Wilkinson, R., Bhargava, S., Giles, P., Romer, A. K., Jeltema, T., Hilton, M., Bermeo, A., Mayers, J., Vergara Cervantes, C., Rozo, E., Rykoff, E. S., Collins, C., Costanzi, M., Everett, S., Liddle, A. R., Mann, R. G., Mantz, A., Rooney, P., Sahlen, M., Stott, J., Viana, P. T. P., Zhang, Y., Annis, J., Avila, S., Brooks, D., Buckley-Geer, E., Burke, D. L., Carnero Rosell, A., Carrasco Kind, M., Carretero, J., Castander, F. J., da Costa, L. N., De Vicente, J., Desai, S., Diehl, H. T., Dietrich, J. P., Doel, P., Flaugher, B., Fosalba, P., Frieman, J., García-Bellido, J., Gaztanaga, E., Gerdes, D. W., Gruen, D., Gruendl, R. A., Gschwend, J., Gutierrez, G., Honscheid, K., James, D. J., Krause, E., Kuehn, K., Kuropatkin, N., Lima, M., Maia, M. A. G., Marshall, J. L., Melchior, P., Menanteau, F., Miquel, R., Ogando, R. L. C.,

Plazas, A. A., Sanchez, E., Scarpine, V., Schubnell, M., Serrano, S., Sevilla-Noarbe, I., Smith, M., Sobreira, F., Suchyta, E., Swanson, M. E. C., Tarle, G., Thomas, D., Tucker, D. L., Vikram, V., Walker, A. R., Weller, J., & DES Collaboration (2019). Mass variance from archival X-ray properties of Dark Energy Survey Year-1 galaxy clusters. , 490(3), 3341–3354.

Flaugher, B., Diehl, H. T., Honscheid, K., Abbott, T. M. C., Alvarez, O., Angstadt, R., Annis, J. T., Antonik, M., Ballester, O., Beaufore, L., Bernstein, G. M., Bernstein, R. A., Bigelow, B., Bonati, M., Boprie, D., Brooks, D., Buckley-Geer, E. J., Campa, J., Cardiel-Sas, L., Castander, F. J., Castilla, J., Cease, H., Cela-Ruiz, J. M., Chappa, S., Chi, E., Cooper, C., da Costa, L. N., Dede, E., Derylo, G., DePoy, D. L., de Vicente, J., Doel, P., Drlica-Wagner, A., Eiting, J., Elliott, A. E., Emes, J., Estrada, J., Fausti Neto, A., Finley, D. A., Flores, R., Frieman, J., Gerdes, D., Gladders, M. D., Gregory, B., Gutierrez, G. R., Hao, J., Holland, S. E., Holm, S., Huffman, D., Jackson, C., James, D. J., Jonas, M., Karcher, A., Karliner, I., Kent, S., Kessler, R., Kozlovsky, M., Kron, R. G., Kubik, D., Kuehn, K., Kuhlmann, S., Kuk, K., Lahav, O., Lathrop, A., Lee, J., Levi, M. E., Lewis, P., Li, T. S., Mandrichenko, I., Marshall, J. L., Martinez, G., Merritt, K. W., Miquel, R., Muñoz, F., Neilsen, E. H., Nichol, R. C., Nord, B., Ogando, R., Olsen, J., Palaio, N., Patton, K., Peoples, J., Plazas, A. A., Rauch, J., Reil, K., Rheault, J. P., Roe, N. A., Rogers, H., Roodman, A., Sanchez, E., Scarpine, V., Schindler, R. H., Schmidt, R., Schmitt, R., Schubnell, M., Schultz, K., Schurter, P., Scott, L., Serrano, S., Shaw, T. M., Smith, R. C., Soares-Santos, M., Stefanik, A., Stuermer, W., Suchyta, E., Sypniewski, A., Tarle, G., Thaler, J., Tighe, R., Tran, C., Tucker, D., Walker, A. R., Wang, G., Watson, M., Weaverdyck, C., Wester, W., Woods, R., Yanny, B., & DES

Collaboration (2015). The Dark Energy Camera. , 150(5), 150.

Fruscione, A., McDowell, J. C., Allen, G. E., Brickhouse, N. S., Burke, D. J., Davis, J. E., Durham, N., Elvis, M., Galle, E. C., Harris, D. E., Huenemoerder, D. P., Houck, J. C., Ishibashi, B., Karovska, M., Nicastro, F., Noble, M. S., Nowak, M. A., Primini, F. A., Siemiginowska, A., Smith, R. K., & Wise, M. (2006). CIAO: Chandra's data analysis system. In D. R. Silva & R. E. Doxsey (Eds.), *Society of Photo-Optical Instrumentation Engineers (SPIE) Conference Series*, volume 6270 of *Society of Photo-Optical Instrumentation Engineers (SPIE) Conference Series* (pp. 62701V).

Hollowood, D. L., Jeltema, T., Chen, X., Farahi, A., Evrard, A., Everett, S., Rozo, E., Rykoff, E., Bernstein, R., Bermeo-Hernandez, A., Eiger, L., Giles, P., Israel, H., Michel, R., Noorali, R., Romer, A. K., Rooney, P., & Splettstoesser, M. (2019). Chandra Follow-up of the SDSS DR8 Redmapper Catalog Using the MATCha Pipeline. , 244(2), 22.

Kelly, B. C. (2007). Some aspects of measurement error in linear regression of astronomical data. *arXiv:0705.2774 [astro-ph]*, (pp. 1–20).

Lahav, O., Calder, L., Mayers, J., & Frieman, J. (2020). *The Dark Energy Survey*. WORLD SCIENTIFIC (EUROPE).

Paul P. Plucinsky, Akos Bogdana, H. L. M. & Tice, N. W. (2018). The complicated evolution of the acis contamination layer over the mission life of the chandra x-ray observatory. *arXiv:1809.02225 [astro-ph.IM]*, (pp. 1–13).

Perlmutter, S., Aldering, G., Goldhaber, G., Knop, R. A., Nugent, P., Castro, P. G., Deustua, S., Fabbro, S., Goobar, A., Groom, D. E., Hook, I. M., Kim, A. G., Kim,

M. Y., Lee, J. C., Nunes, N. J., Pain, R., Pennypacker, C. R., Quimby, R., Lidman, C., Ellis, R. S., Irwin, M., McMahon, R. G., Ruiz-Lapuente, P., Walton, N., Schaefer, B., Boyle, B. J., Filippenko, A. V., Matheson, T., Fruchter, A. S., Panagia, N., Newberg, H. J. M., Couch, W. J., & Project, T. S. C. (1999). Measurements of Ω and Λ from 42 High-Redshift Supernovae. , 517(2), 565–586.

Riess, A. G., Filippenko, A. V., Challis, P., Clocchiatti, A., Diercks, A., Garnavich, P. M., Gilliland, R. L., Hogan, C. J., Jha, S., Kirshner, R. P., Leibundgut, B., Phillips, M. M., Reiss, D., Schmidt, B. P., Schommer, R. A., Smith, R. C., Spyromilio, J., Stubbs, C., Suntzeff, N. B., & Tonry, J. (1998). Observational Evidence from Supernovae for an Accelerating Universe and a Cosmological Constant. , 116(3), 1009–1038.

Rykoff, E. S., Rozo, E., Busha, M. T., Cunha, C. E., Finoguenov, A., Evrard, A., Hao, J., Koester, B. P., Leauthaud, A., Nord, B., Pierre, M., Reddick, R., Sadibekova, T., Sheldon, E. S., & Wechsler, R. H. (2014). redMaPPer. I. Algorithm and SDSS DR8 Catalog. , 785(2), 104.

Rykoff, E. S., Rozo, E., Hollowood, D., Bermeo-Hernandez, A., Jeltema, T., Mayers, J., Romer, A. K., Rooney, P., Saro, A., Vergara Cervantes, C., Wechsler, R. H., Wilcox, H., Abbott, T. M. C., Abdalla, F. B., Allam, S., Annis, J., Benoit-Lévy, A., Bernstein, G. M., Bertin, E., Brooks, D., Burke, D. L., Capozzi, D., Carnero Rosell, A., Carrasco Kind, M., Castander, F. J., Childress, M., Collins, C. A., Cunha, C. E., D'Andrea, C. B., da Costa, L. N., Davis, T. M., Desai, S., Diehl, H. T., Dietrich, J. P., Doel, P., Evrard, A. E., Finley, D. A., Flaugher, B., Fosalba, P., Frieman, J., Glazebrook, K., Goldstein, D. A., Gruen, D., Gruendl, R. A., Gutierrez, G., Hilton, M., Honscheid, K., Hoyle, B.,

James, D. J., Kay, S. T., Kuehn, K., Kuropatkin, N., Lahav, O., Lewis, G. F., Lidman, C., Lima, M., Maia, M. A. G., Mann, R. G., Marshall, J. L., Martini, P., Melchior, P., Miller, C. J., Miquel, R., Mohr, J. J., Nichol, R. C., Nord, B., Ogando, R., Plazas, A. A., Reil, K., Sahlén, M., Sanchez, E., Santiago, B., Scarpine, V., Schubnell, M., Sevilla-Noarbe, I., Smith, R. C., Soares-Santos, M., Sobreira, F., Stott, J. P., Suchyta, E., Swanson, M. E. C., Tarle, G., Thomas, D., Tucker, D., Uddin, S., Viana, P. T. P., Vikram, V., Walker, A. R., Zhang, Y., & DES Collaboration (2016). The RedMaPPer Galaxy Cluster Catalog From DES Science Verification Data. , 224(1), 1.

Voit, G. (2005). Tracing cosmic evolution with clusters of galaxies. *Reviews of Modern Physics*, 77, 207–258.

Wu, H.-Y., Rozo, E., & Wechsler, R. H. (2010). Annealing a Follow-up Program: Improvement of the Dark Energy Figure of Merit for Optical Galaxy Cluster Surveys. , 713(2), 1207–1218.

Zhang, Y., Yanny, B., Palmese, A., Gruen, D., To, C., Rykoff, E. S., Leung, Y., Collins, C., Hilton, M., Abbott, T. M. C., Annis, J., Avila, S., Bertin, E., Brooks, D., Burke, D. L., Carnero Rosell, A., Carrasco Kind, M., Carretero, J., Cunha, C. E., D'Andrea, C. B., da Costa, L. N., De Vicente, J., Desai, S., Diehl, H. T., Dietrich, J. P., Doel, P., Drlica-Wagner, A., Eifler, T. F., Evrard, A. E., Flaugher, B., Fosalba, P., Frieman, J., García-Bellido, J., Gaztanaga, E., Gerdes, D. W., Gruendl, R. A., Gschwend, J., Gutierrez, G., Hartley, W. G., Hollowood, D. L., Honscheid, K., Hoyle, B., James, D. J., Jeltema, T., Kuehn, K., Kuropatkin, N., Li, T. S., Lima, M., Maia, M. A. G., March, M., Marshall, J. L., Melchior, P., Menanteau, F., Miller, C. J., Miquel, R., Mohr, J. J.,

Ogando, R. L. C., Plazas, A. A., Romer, A. K., Sanchez, E., Scarpine, V., Schubnell, M., Serrano, S., Sevilla-Noarbe, I., Smith, M., Soares-Santos, M., Sobreira, F., Suchyta, E., Swanson, M. E. C., Tarle, G., Thomas, D., Wester, W., & DES Collaboration (2019). Dark Energy Survey Year 1 Results: Detection of Intracluster Light at Redshift ˜ 0.25. , 874(2), 165.